ACSNANO

www.acsnano.org

ARTICLE

Simultaneous, Single-Particle Measurements of Size and Loading Give Insights into the Structure of Drug-Delivery Nanoparticles

Albert Kamanzi,[○] Yifei Gu,[○] Radin Tahvildari,[○] Zachary Friedenberger, Xingqi Zhu, Romain Berti, Marty Kurylowicz, Dominik Witzigmann, Jayesh A. Kulkarni, Jerry Leung, John Andersson, Andreas Dahlin, Fredrik Höök, Mark Sutton, Pieter R. Cullis, and Sabrina Leslie*

Cite This: https://doi.org/10.1021/acsnano.1c04862

Read Online

ACCESS | Metrics & More | Article Recommendations | Supporting Information

ABSTRACT: Nanoparticles are a promising solution for delivery of a wide range of medicines and vaccines. Optimizing their design depends on being able to resolve, understand, and predict biophysical and therapeutic properties, as a function of design parameters. While existing tools have made great progress, gaps in understanding remain because of the inability to make detailed measurements of multiple correlated properties. Typically, an average measurement is made across a heterogeneous population, obscuring potentially important information. In this work, we develop and apply a method for characterizing nanoparticles with single-particle resolution. We use convex lens-induced confinement (CLiC) microscopy to isolate and quantify the diffusive trajectories and fluorescent intensities of individual nanoparticles trapped in microwells for long times. First, we benchmark detailed measurements of fluorescent polystyrene nanoparticles against prior data to validate our approach. Second, we apply our method to investigate the size and loading properties of lipid nanoparticle (LNP) vehicles containing silencing RNA (siRNA), as a function of lipid formulation, solution pH, and drug-loading. By taking a comprehensive look at the correlation between the intensity and size measurements, we gain insights into LNP structure and how the siRNA is distributed in the LNP. Beyond introducing an analytic for size and loading, this work allows for future studies of dynamics with single-particle resolution, such as LNP fusion and drug-release kinetics. The prime contribution of this work is to better understand the connections between microscopic and macroscopic properties of drug-delivery vehicles, enabling and accelerating their discovery and development.

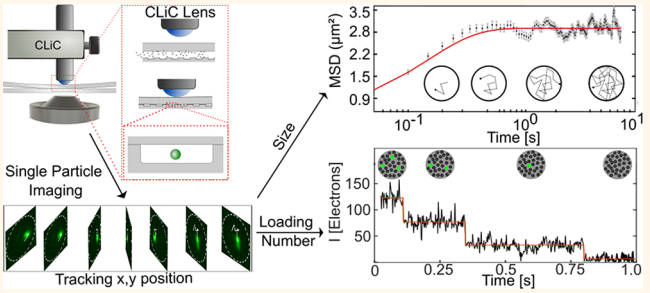

KEYWORDS: *lipid nanoparticles, single-molecule, drug-delivery, vaccines, genetic medicines, nanomedicines, microscopy*

Downloaded via UNIV OF BRITISH COLUMBIA on December 3, 2021 at 23:21:32 (UTC).
See https://pubs.acs.org/sharingguidelines for options on how to legitimately share published articles.

Nanocarriers and nanoparticles are increasingly used in medicine as vehicles for functional cargo. Broadly speaking these vehicles include micelles, liposomes, nanoemulsions, as well as lipid, polymeric, and dendritic nanoparticles, which exhibit a variety of useful properties including biopersistence, targeting, enhanced cellular penetration, stimuli-sensitivity, and direct carrier visualization.[1] Lipid-based nanoparticles (LNPs)[2] have been developed to deliver a rapidly growing class of genetic medicines,[3−5] including silencing RNAs (siRNAs), messenger RNAs (mRNAs), and other biologics, with growing importance. LNPs aid delivery of these molecules by preventing degradation in biological fluids,[3] improving transit across cell membranes and providing targeted and concentrated delivery.[4] Furthermore, LNPs exhibit a number of desirable characteristics, such as ease of manufacture, lack of immune response, high carrying capacity, and can be dosed repeatedly.[6]

LNPs made from ionizable cationic lipids have been successful as delivery vehicles for mRNA vaccines,[7] including Covid-19 vaccines.[8,9] It has also been shown that LNPs may effectively deliver large mRNA-based drugs in the context of gene therapy.[9,10] The ionizable cationic lipids are especially suited for these applications, as their properties have been tuned to have several advantages, including: increased loading

Received: June 7, 2021
Accepted: October 21, 2021

© XXXX American Chemical Society

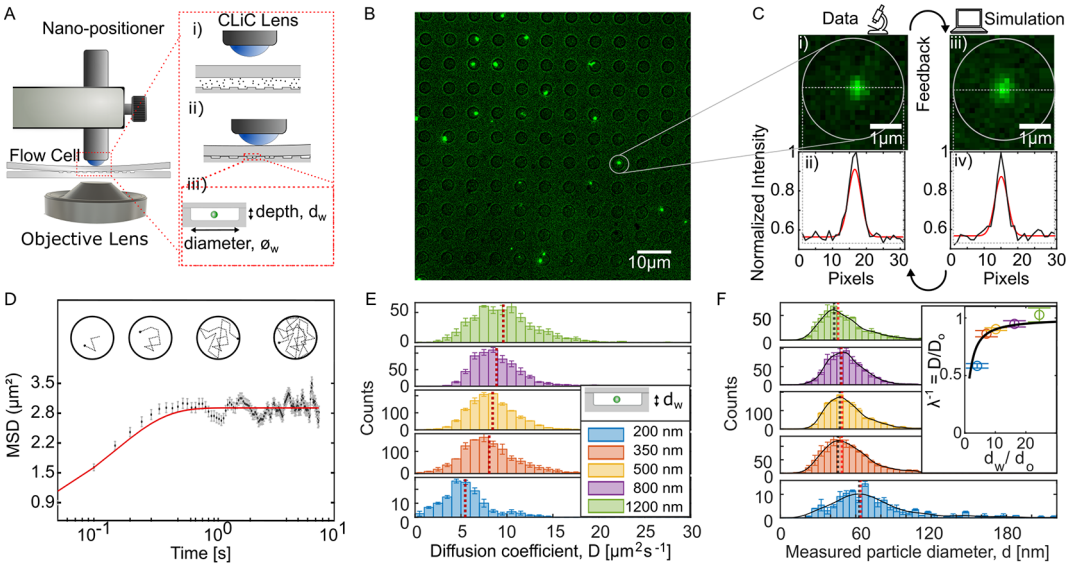

Figure 1. CLiC nanoparticle characterization assay. (A) Schematic of the CLiC instrument and cross section of a flow cell. (i) The curved CLiC lens deflects the top surface downward (ii) and traps sample in the microwells embedded in the bottom surface of the flow cell (iii). (B) Image of fluorescently labeled 24 nm radius polystyrene particles in an array of 3 μm diameter microwells. (C) A close-up image of a single NP inside a 3 μm microwell, with cross section and fitting curve inset, and comparison to simulations. Microscopy data are shown on the left (i) and (ii) and was obtained under 100× magnification with 160 nm/pixel resolution. Simulation data are shown on the right (iii) and (iv). (D) Particle tracking is used to construct the confined-MSD curve for each LNP, described in Materials and Methods and SI. The red line is the fitted theoretical model (eq 1) to the experimental data (back point with error bars). (Inserts) Confined particle diffusion is shown over time, illustrating that the shoulder in the MSD curve relates to the finite area of the microwell. (E) Individual NP diffusivities are extracted from fitting each curve in (D) and compiled into a distribution for the measured population. Diffusivity distributions are measured for NPs confined in microwells with 200, 350, 500, 800, and 1200 nm depths and 10 μm diameter. The distributions in (E) and (F) represent averaged measurements from at least 2−3 experiments, where each bar plot was obtained by averaging bins of the corresponding histograms. (F) To account for hydrodynamic effects at the walls of the microwell, we use a modified Stokes−Einstein equation described by eq 2 to correct for confinement geometry. This collapses the different diffusivity distributions onto a single size distribution, except for the case of 200 nm depth. The size of the particle is obtained by fitting the measured diffusion coefficient values to a theoretical model (eq 3) as shown in (F insert) and was found to be 49 ± 6 nm. All the dashed lines are summarized in Table 2 of SI.

efficiency during their formation[11] as a result of lipid-drug charge interactions, which simultaneously promotes the self-assembly of the nanoparticles; reduced toxicity during transport, as a result of lowered surface charge of the nanoparticles;[12] and optimized drug delivery following endocytosis to the target cells.[11] Additionally, ionizable lipids are generally found to be non-immunogenic and non-oncogenic and have minimal cytotoxicity compared to other delivery vectors.[13] Optimizing their formulation parameters involves tuning the acid dissociation constants (pK_a) of the ionizable cationic lipids to values in the range of 6.2−6.7.[11]

Despite the promise of LNPs as drug-delivery vehicles, there are significant challenges to overcome in their optimization, especially with regard to efficiency of delivery and uptake in cells. A broad range of methods are available for characterizing nanoparticles, including dynamic light scattering (DLS), nanoparticle tracking analysis (NTA), atomic force microscopy (AFM), cryogenic transmission electron microscopy (cryo-TEM), flow cytometry (FCM), resistive pulse sensing (RPS), and quartz crystal microbalance with dissipation (QCM-D). These techniques have provided valuable insights into the physical characteristics of nanoparticle samples, but since microscopic properties of the LNPs, including particle size, structure, cargo-loading, and surface chemistry, are often heterogeneous,[7] each of these methods has limitations (see Table 1 and discussion in SI) and leave important gaps even when used in combination. The available techniques are either bulk measurements and lack single-particle resolution (DLS, FCM), or have single-particle resolution for very short times (NTA, RPS), or require surface immobilization to achieve longer times (AFM, cryo-EM), which can bias results by altering particle structure and hence cannot be applied to studying sample dynamics. What is missing, and what this work addresses, is a platform for tether-free, single-particle measurements with sufficiently long per-particle observation times in cell-like conditions as well as the capacity to change conditions and image the response.

In this work, we introduce a multiparametric nanoparticle imaging platform capable of imaging many individually confined nanoparticles which are diffusing in controlled solution conditions. This platform uses the convex lens-induced confinement (CLiC) microscopy technique[14−16] which has been applied to study confined DNA and polymers,[17−19] DNA plasmids[20,21] and proteins,[22] as well as their responses to changes in solution conditions.

Integral to this platform, we develop simulations of model data crucial for obtaining precise and accurate measurements and analysis. These analysis tools inform a dynamic "feedback loop" which optimizes the selection of parameters for data acquisition and analysis, customized for a given molecular sample, in order to minimize the statistical and systematic error in the size and loading measurements. To inform this platform, we develop a robust theoretical treatment of the effect of micro/nanoscale confinement on the imaged diffusivity of the nanoparticles in the CLiC device and take these effects into account in interpreting nanoparticle size.

https://doi.org/10.1021/acsnano.1c04862
ACS Nano XXXX, XXX, XXX−XXX

To establish and validate our multiparametric platform, we first study polystyrene nanoparticles of known size, measuring their diffusivity and size distributions under a range of confinement conditions. We then use this platform to investigate more complex biological samples of lipid nanoparticles (LNPs) with less-understood size and loading characteristics. Here, we investigate changes in (nonloaded) LNP structures as a function of pH and ionizable lipid composition and take a detailed look at how LNP size and structure change once the LNPs are loaded with siRNA. Significantly, the ability to simultaneously measure both size and siRNA-loading of individual LNPs enables a scaling analysis which reveals the spatial distribution of siRNA cargo within the LNP. The ability to measure size and loading simultaneously as well as the dynamic changes of these variables at the single-particle level is important for designing multifunctional LNPs for drug delivery. Our method can be developed further to imaging LNP dynamics at the interface of and inside cells.

RESULTS AND DISCUSSION

Validation of Single-Particle Diffusivity and Size Analytic Measurement Using 48 nm Diameter Polystyrene Nanoparticles. We demonstrate the sizing and simulation components of our method using measurements of carboxylate-modified microspheres composed of polystyrene, from ThermoFisher.[23] We chose 48 nm polystyrene nanoparticles to match the diameter of the LNPs presented later in this paper. Figure 1 shows the flow of experimental and analytic steps which transform a sequence of CLiC images of diffusing nanoparticles into a distribution of individually measured diffusivities and sizes.

Figure 1A shows a schematic of the CliC imaging device, which holds a flow-cell containing embedded microwells and is mounted on an inverted microscope. A suspension of nanoparticles is introduced in the flow-cell (~30 μm deep, Figure 1(i)) using a microfluidic chuck. The CliC lens is controlled by a nanopositioner, deflecting the top of the flow cell downward to confine the suspension within the array of microwells, as shown in Figure 1(ii,iii). The seal formed between the glass surfaces excludes out-of-focus material which enables sensitive detection of single diffusing nanoparticles.

Figure 1B shows a series of fluorescence images of nanoparticles trapped in an array of ~100 microwells (3 μm diameter and 500 nm depth) in an 82 μm × 82 μm field of view. The concentration of nanoparticles is approximately 1 nM, which results in trapping an average of one nanoparticle per well and is convenient for analysis. Serial measurements are made by raising and lowering the CliC lens and replenishing the array of wells with fresh nanoparticles from the bulk volume of the flow-cell chamber so that thousands of single particle trajectories can be obtained in a relatively short time (*i.e.*, 1−3 h with the current implementation). In this way, the CliC method provides sensitive, single-particle measurements with good statistics and a number of advantages including the ability to replenish the sample in an array of wells using the CliC actuator, tune the sample concentration so there is one particle per well on average, and use information from other wells to improve the analysis (*i.e.*, empty wells to establish the local background and excluding wells with stuck or aggregated molecules such that calculations are performed exclusively on freely diffusing particles).

Figure 1C shows an image of a single microwell, in which a single particle is a diffraction-limited spot. Its trajectory (x, y position) is recorded over the course of many sequential images using particle-tracking software (see SI, Particle detection, tracking, and sizing for details). Imaging and experimental parameters include exposure time per frame, number of frames, laser intensity, dimension and number of wells per field of view, sample concentration, and number of trajectories per data set.

The selection of these parameters is informed by an iterative process which generates simulations of diffusing nanoparticles under confinement, using these input parameters, analyzes the simulated data to assess the statistical and systematic error on the output size and intensity measurements, and iterates on these parameters to reduce these errors to be below an acceptable bound (see Materials and Methods and SI Simulation of confined particles).

The mean square displacement (MSD) curve is constructed for each particle trajectory (Figure 1D). The diffusion coefficient for every particle is determined by fitting this curve to the analytical expression derived for the MSD under the confined conditions:[43,44]

$$\mathrm{MSD}(t) = O + r^2\left(1 - 8\sum_{m=1}^{\infty}\frac{e^{[-\alpha_{1m}^2 t/\tau]}}{\alpha_{1m}^2(\alpha_{1m}^2 - 1)}\right) \quad (1)$$

where O is the offset, r is the confinement radius, $\tau = \frac{r^2}{D}$ is the characteristic time scale, D is the diffusion coefficient, and α_{1m} is the m^{th} positive root of the derivative of the Bessel function of the first kind (see Materials and Methods and SI, Simulation of confined particles). Figure 1E shows the distribution of measured diffusion coefficients for the sampled population under a range of confinement depths. The measured diffusivity is lower for the same nanoparticles under more constrained conditions due to hydrodynamic effects near confining surfaces.[24−26] For these measurements, this effect is <15% for wells with heights between 200 and 1200 nm and fixed diameter of 10 μm, as shown in the inset of Figure 1F.

To convert diffusivity to size distributions, we use a modified Stokes−Einstein relation:[24]

$$D_{\parallel} = \frac{k_B T}{6\pi\eta\lambda a} = \lambda^{-1} D_0 \quad (2)$$

where $D_{\parallel}$ is the diffusivity of particles near two parallel confining planes, D_0 is the diffusivity in bulk, k_B is the Boltzmann constant, T is the temperature, η is the kinetic viscosity of the solution, and a is the hydrodynamic radius. Λ is a correction factor used to account for the hydrodynamic effects near surfaces (see Materials and Methods).[24−26] We obtain the correction factor (λ) for each confinement depth by fitting the diffusion coefficients to a theoretical model given by eq 2. After this correction, we observe the diffusivity distributions acquired under different confinement conditions to converge to the same size distribution (Figure 1F), with a peak at 49 ± 6 nm diameter in agreement with the manufacturer's specifications (48 ± 0.6 nm diameter).[23] This validates our characterization method for particle size, including the necessary simulation and theoretical tools to account for confined diffusion of hard spheres near surfaces.

Probing Structural Transition in Unloaded LNPs, Induced by Changing Buffer Conditions (pH). We apply our single-molecule methodology to investigate the impact of

https://doi.org/10.1021/acsnano.1c04862
ACS Nano XXXX, XXX, XXX−XXX

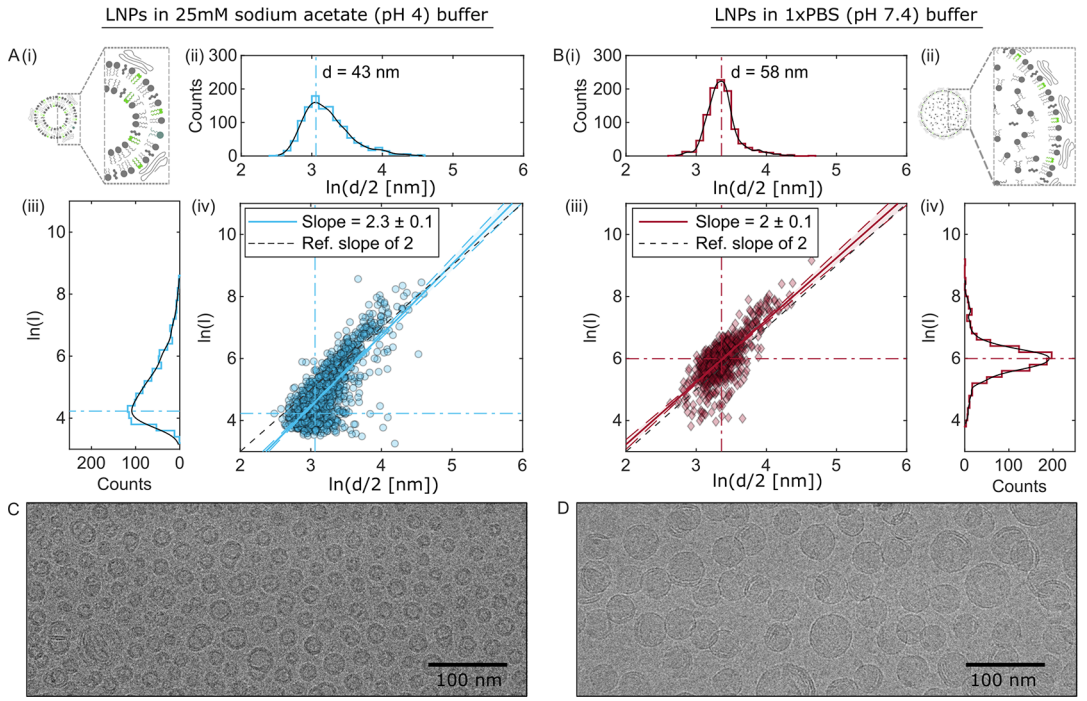

Figure 2. LNP structural modifications as a function of pH. Measurements of LNPs in pH 4/pH 7.4 buffer conditions (25 mM NaOAc)/(1× PBS) are shown in blue/red (A/B). Size (A(ii), B(i)) and fluorescence intensity (A(iii), B(iv)) distributions for LNP populations at pH 4 and pH 7.4, respectively, are projected onto a log−log scatter plot (A(iv), B(iii)). Counts refers to number of particles. Linear fits to the correlated data indicate the scaling of intensity with radius. The scaling coefficient gives information about the expected distribution of fluorophores within the LNP structure. For example, if intensity scales as radius raised to the power of two (or three), the fluorophores would reside on the surface (or in the volume). Schematics of the LNP structures and spatial distribution of fluorophores are shown in A(i) and B(ii), respectively. Reproduced based on schematics in ref 27. Corresponding cryo-TEM images of the LNPs are shown in C (pH 4) and D (pH 7.4). For LNPs formed in the pH 7.4 solution, the fluorophores are expected to be excluded from the LNP volume and be present only on outermost surface of the LNP. This is consistent with the observed scaling between intensity and radius raised to the power of two (shown in red). For LNPs formed in the pH 4 solution, bilayer structures are expected in which the fluorophores can be integrated, which may correspond to a layer around 5−6 nm thick based on prior work. This is consistent with the observed scaling coefficient between two and three (shown in blue), when the log−log scatter plot is fit over a large range of radii.

buffer pH on the biophysical properties of LNPs. For this, we use the LNP formulation based on Onpattro (patisiran), the first FDA-approved LNP-based drug. The LNPs are composed of ionizable lipid 2,2-dilinoleyl-4-(2-dimethylaminoethyl)[1,3]-dioxolane[12] (Dlin-KC2-DMA or KC2), cholesterol (Chol), as well as two structural lipids: distearolyphosphatidycholine (DSPC) and PEG-lipid (DSPE-PEG2000). We produce nanoparticles at pH 4 using an established rapid mixing method, described in refs 6, 27, and 28 at a mixing ratio of KC2/Chol/DSPC/PEG-lipid (50/39/10/1 mol % respectively). We then generate nanoparticles at pH 7.4, by taking the above LNPs suspended in the pH 4 sodium acetate buffer (25 mM NaOAc) and dialyzing them into a pH 7.4 phosphate-buffered saline solution (1× PBS). This induces a fusion process that results in the formation of a different nanoparticle structure.[29]

Figure 2 illustrates a previously proposed change in particle structure from a small bilayer LNP at pH 4 (Figure 2 A(i)) to a larger particle with an oil droplet core surrounded by a lipid monolayer shell at pH 7.4, with cryo-TEM measurements[27,30] (Figure 2 B(ii)). The structural transitions and LNP formation process are driven by neutralization of the ionizable lipids and is thought to be essential to the complete formation of LNP systems. The pK_a of the ionizable lipids (6.7 for KC2) has been tuned to optimize the LNPs' entrapment of nucleic acid loads as well as their intracellular delivery.[3,9]

For our single-particle fluorescence imaging experiments, we label nanoparticles with lipophilic fluorescent dyes DiI-C18, a dialkyl-carbocyanine[49] derivative commonly known as DiI, at a labeling ratio of 1%. This dye is incorporated into the LNP during particle formation, and only weakly fluoresces when not incorporated into the membrane. Additionally, it is essentially completely water insoluble and hence prefers to reside inside the LNP membrane structures. This allows us to simultaneously measure the spatial trajectory and fluorescence intensity of individual LNPs. DiI has a polar structure with a hydrophilic headgroup attached to hydrophobic tail chains, which are expected to insert into the LNP surface membrane. Our measurements use approximately 26 dyes per LNP, inserted so as to randomly sample the outer surface.

By compiling many single-particle measurements, we establish the distributions of size and intensity for the LNP population, as shown in Figure 2A(ii,iii),B(i,iv). The size distributions are the result of a full diffusivity analysis as described above, including corrections for confinement (details shown in Table 2 of SI). Our results show an increase in both particle size and intensity as a function of increased pH. The size distribution probes important properties of the nanoparticles, such as monodispersity which is hypothesized to help with cell-uptake once the particle size is optimized, and self-affinity or tendency for aggregation which may lower therapeutic effectiveness.

https://doi.org/10.1021/acsnano.1c04862
ACS Nano XXXX, XXX, XXX−XXX

Figure 2A(iv),B(iii) shows scatter plots combining both of these distributions, where each point represents the size and intensity of a single LNP. By fitting log−log plots with linear regression, we obtain a slope of 2.0 ± 0.1 for LNPs at pH 7.4 and a higher slope 2.3 ± 0.1 for LNPs at pH 4. The corresponding R^2 values for the fitting are 0.54 and 0.60 respectively, and the *p*-values for the fitting, with *t*-statistic null hypothesis testing, are both below 0.05. Hence the linear regressions are good representations for the data. The intensity to radius scaling coefficient gives us important information about the expected distribution of fluorophores within an LNP structure. Our result at pH 7.4 is consistent with fluorescent dyes inserted into the surface of the LNPs, resulting in particle brightness that scales as surface area of a particle (Figure 2B(ii)). On the other hand, the higher scaling slope observed at pH 4 is consistent with the dye distribution being partially on the outer surface as well as in the volume of the LNP (*i.e.*, inner surface of bilayer). This can be explained by the presence of DiI molecules on the inner surface of the bilayer membrane structure of the (smaller) nanoparticles, as shown in the schematic of Figure 2A(i).

Our measurements are sensitive to the available lipid-aqueous interface per LNP, and as a result, we can use DiI labels to directly extract structural information for the nanoparticles. These results are also consistent with cryo-TEM measurements—performed on similar samples—as shown in Figure 2C,D.

Control Measurements: Bilayer LNPs without Ionizable Lipids, in pH 7.4 Buffer. To further validate our measurements, we use the same approach to measure the size and fluorescent dye loading of nanoparticles with no ionizable lipids in their composition, as a control sample with no additional complexity arising from charge or ionization effects. These LNPs have no drug encapsulated and were formulated as described in Materials and Methods using Chol/DSPC/PEG-lipid compositions at a mixing ratio of (39/56/5 mol % respectively), where the structural lipid components are increased to replace the KC2 component. In this case, the nanoparticles are known to maintain their bilayer structure in both buffer conditions.

Figure 3B,C shows the fluorescence intensity and size distributions for the control LNPs in pH 7.4 buffer conditions. In Figure 3D, these distributions are projected onto a log−log scatter plot. Again, a linear regression fit to the data is used to measure the scaling of fluorescence intensity with particle size. In this case, the scaling exponent is 2.2 ± 0.1, indicative of fluorophores partially filling the volume of the sphere. The corresponding R^2 values for the fitting is 0.70, and *p*-value for the fitting, with *t*-statistic null hypothesis testing, is below 0.05 and validates the linear regression.

The difference in the scaling coefficients for the two bilayer LNPs (Figures 2A and 3) can be explained by the difference in relative size of the bilayer thickness (*e.g.*, 5−6 nm) with respect to radius of the particle (*e.g.*, 20−30 nm). For smaller particles, the relative volumetric contribution of dyes in the bilayer can be more significant, since the finite bilayer thickness occupies more of the sample volume, which means that the observed scaling coefficient will be >2. By contrast, for larger particles and with a smaller relative bilayer thickness, the scaling of the intensity with radius will more closely approach a power of two.

Additional *t*-statistic hypothesis testing was performed to compare the 3 different measurements for linear regression

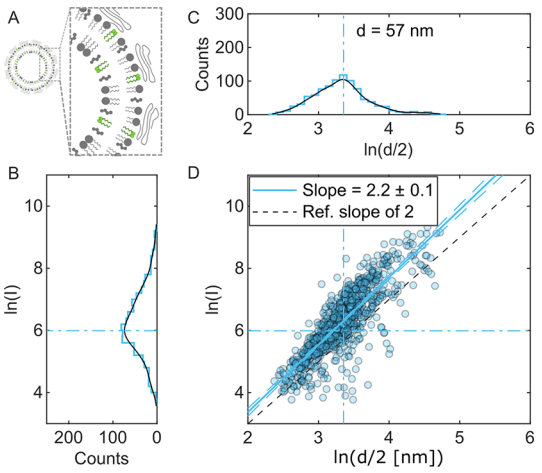

Figure 3. Control lipid nanoparticles: Measurements on unloaded neutral LNP, with no ionizable lipids in their formulation. (A) Schematic of the neutral LNPs, showing a bilayer structure as well as a layer of the PEG brushes. Size (B) and fluorescence intensity (c) distributions for the LNP are projected onto a log−log scatter plot (D). Counts refers to number of particles. A linear fit to the correlated data indicate the scaling of intensity with radius. The fitting was performed using MatLab's linear regression model and resulted in an R^2 value of 0.768. Similar to the pH 4 ionizable LNP samples in Figure 2, the fluorophores are able to reside on both surfaces of the bilayer, hence resulting a radius-intensity scaling >2.

slopes. The corresponding *p*-values obtained were all below 0.03 (3.2×10^{-7} for pH 4 *vs* pH 7.4 samples, 6.6×10^{-4} for pH 7.4 *vs* control samples, and 0.03 for pH 4 *vs* control sample). Hence the differences are significant with 97% confidence or more.

Quantification of siRNA Drug Loading with Single-Molecule Resolution. To study cargo loading of the nanoparticles, we again use LNPs with a formulation based on that of the Onpattro (patisiran) drug. In this case, the nanoparticles were loaded with siRNA molecules chosen to achieve amino lipid nitrogen-to-siRNA phosphate (N/P) charge ratio of 3. This formulation is expected to result in the loading of hundreds of siRNA molecules per LNP, as estimated from the mixing ratios. For these, fluorescent dyes Ty563 were covalently bonded to the siRNA molecule, and the labeling fraction was varied for different experiments.

To analyze siRNA loading in the LNPs, we use two complementary methods. The first is a photobleaching analysis (Figures 4 and 5), where the number of fluorophores is counted using the number of photobleaching steps. To optimally resolve consecutive bleaching events of individual fluorophores, this requires high signal-to-noise per fluorophore with short exposure times (low fluorophore loading and high laser intensity).

The second method uses the particle-tracking size and intensity analysis described above. This benefits from high fluorophore loading and low laser power to obtain long single-particle trajectories, in order to improve the signal-to-noise of the measurements of diffusivity and size (Figure 6). Applying both methods to characterize a given LNP-drug construct gives consistent results.

Three representative intensity traces are shown in Figure 4A,D,G, in which single LNPs undergo stepwise photobleaching. The solid colored lines show fitting for the mean of

https://doi.org/10.1021/acsnano.1c04862
ACS Nano XXXX, XXX, XXX−XXX

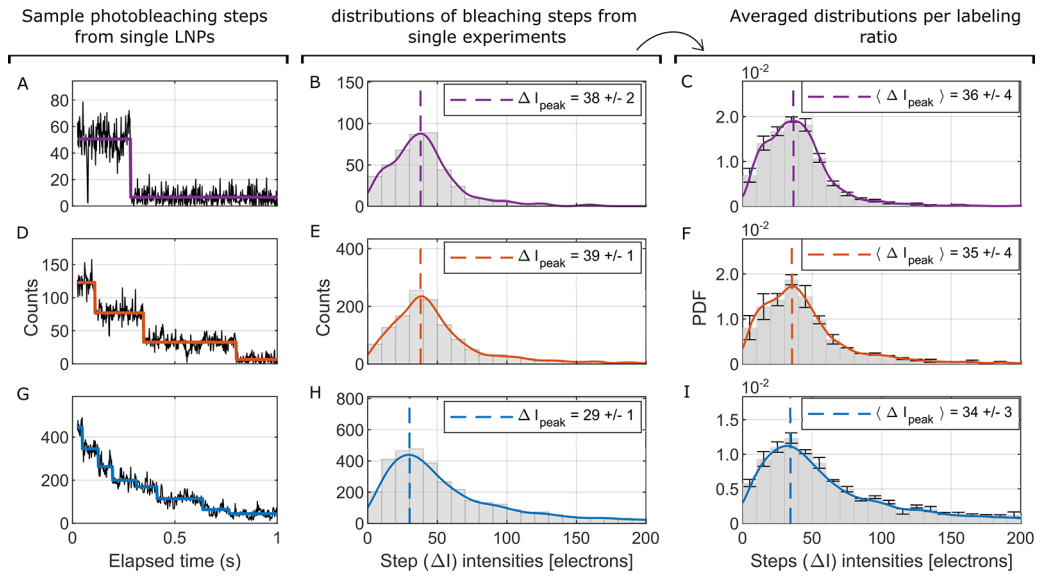

Figure 4. Photobleaching analysis of siRNA-loaded LNPs to measure single dye intensities. Left column: (A), (D), and (G) Sample intensity traces, with discrete photobleaching steps, for samples labeled with 1, 3, and 10 fluorophores per LNP, respectively. Middle column: (B), (E), and (H) Step-size distributions, from single experiments, with kernel density fits to obtain maximum likelihood step intensity. Right column: (C), (F), and (I) Averaged step intensity distributions for the 3 different samples. The bar chart is obtained by averaging corresponding histogram bins, to obtain a mean distribution, with error bars. The dashed lines represent an average of peak intensities from different experiments, and lines up nicely with a fitted kernel density.

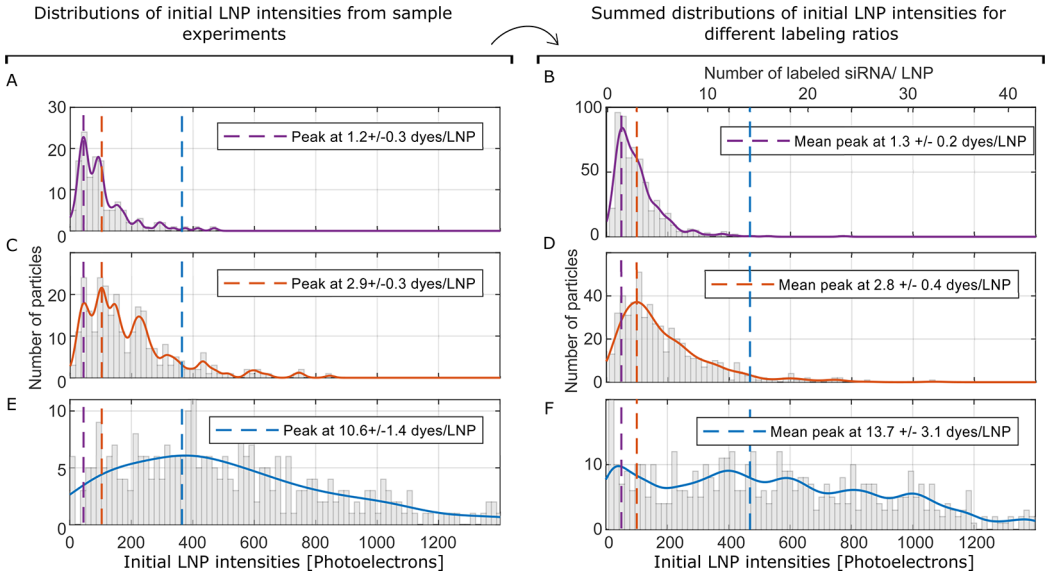

Figure 5. LNP drug loading (siRNA) measurements with single-molecule resolution. Left column: (A), (C), and (E) Distributions of initial particle intensities, before photobleaching, from sample experiments. Kernel density fits to the data are used to obtain peak intensities. Right column: (B), (D), and (F) Pooled distributions of the initial intensities. The dashed lines represent average of peak intensities from different experiments, which line up well with kernel density fits to the data.

the discrete intensity levels. The fitting is performed with the photobleaching detection algorithm reported by Chen *et al.*,[31] which uses the two-sample t test to determine the discrete plateau regions in the intensity traces. Each intensity step corresponds to a single photobleaching event. An example of a fitted step is indicated by ΔI in Figure 4A. Distributions of step sizes, from individual experiments, are shown in Figure 4B,E,H, for each of the 3 labeling ratios. The colored lines show fitting with a kernel density estimation for the maximum likelihood step intensity, as described in Materials and Methods. The fitted peak intensities are shown by a dashed line. The KDE models were fitted using a bootstrapping statistical method, allowing us to obtain uncertainties in the fitted step intensities (see SI, LNP cargo-loading distributions, for details).

Figure 4C,F,I shows the average distributions of the step intensities, with error bars calculated from the standard deviation of values replica experiments (at least 2−3 experiments were performed per labeling ratio). The dashed lines represent average of peak intensities (36 ± 2, 35 ± 4, and 33 ± 2 photoelectrons for the 1, 3, and 10 fluorophores/LNP samples), corresponding to the intensity of a single dye. These mean intensities line up well with peaks from kernel density fitting to the distributions. We observe that higher fluorophore loading can lead to a wider step-size distribution due to some

https://doi.org/10.1021/acsnano.1c04862
ACS Nano XXXX, XXX, XXX−XXX

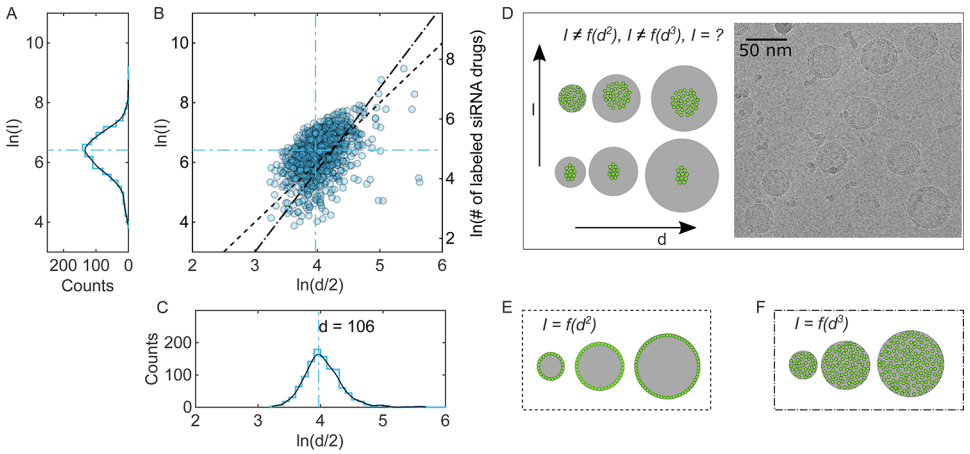

Figure 6. siRNA drug distribution in LNPs. Measured fluorescence intensity (A) and size (C) distributions for populations of LNPs formulated with siRNA drugs are projected onto a log−log scatter plot (B); reference (black dotted/dashed) lines correspond to potential scaling coefficients between intensity and radius (squared/cubed), in scenarios where the siRNA is uniformly loaded (on the surface/within the volume). A secondary axis shows the drug loading for the nanoparticles and was obtained by converting the particle intensities to drug loading numbers, as described in the SI (see LNP cargo-loading distributions for details). Schematics of three possible distributions of the siRNA drug inside the nanoparticles: uncorrelated (D); surface-loaded (E); and volume-filled (F). The acquired data are consistent with uncorrelated loading. (D) Also shows a cryo-TEM image, taken with similar samples.

steps catching more than one fluorophore bleaching event in the same exposure time.

Figure 5 shows the initial intensities of the nanoparticles before photobleaching. The left column of Figure 5A,C,E shows distributions from individual experiments, with kernel density fitting for the maximum likelihood particle intensities. The right column of Figure 5B,D,F shows the combined distributions of all replicas per labeling ratio. Mean initial particle intensities are calculated from the corresponding experiments and are shown by dashed lines. We convert these distributions to labeled drug loading numbers using the measured bleaching steps in Figure 4 listed above, to obtain mean peak loading per labeling ratio (1.3 ± 0.2, 2.8 ± 0.4, and 13.7 ± 3.1 labeled siRNA molecules for the same 3 samples with nominally 1, 3, and 10 fluorophore/LNP loading as calculated from formulation fractions). Again, kernel density fitting curves are in good agreement with the measured mean loading per sample.

Simultaneous Size and Loading Measurements of LNPs Containing siRNA Drugs. Figure 6 shows the size and intensity analysis of siRNA-loaded nanoparticles, with the same formulation as used above. The nanoparticles were loaded with hundreds of siRNA molecules per LNP (estimated to be 200−400 molecules/LNP), where ∼100 siRNA molecules per LNP were tagged with Tye563 fluorescent dyes. The labeled siRNA molecules were purchased from Integrated DNA Technologies.[50] The lipid components were kept the same as those in Figure 2, and the nanoparticles were imaged in pH 7.4 buffer conditions.

The measured per-particle size (Figure 6C) and fluorescence intensity (Figure 6A) distributions are shown projected on a log−log plot in Figure 6B for the siRNA loaded LNPs at pH 7.4. The left side (primary axis) shows loading values as measured in intensity units. A right side (secondary) axis is obtained by calibrating single dye intensities for the measurements in Figure 6, as described in the SI (see LNP cargo-loading distributions for details). Interestingly, the scatter plot for the loaded sample does not show strong correlation between intensity and particle size, especially when viewed in comparison to the unloaded data in Figure 2. Specifically, while the unloaded LNPs are characterized by a similar spread in size, their intensity has larger relative spread and falls closer to a linear regression line. This qualitative difference in the two scatter plots provides insight into how the siRNA are distributed inside the LNPs. For instance, our measurements are not consistent with two candidate distributions: a shell-like distribution where the siRNA molecules are embedded between two pairs of bilayers inside the particle (Figure 6E), or a volume-filled distribution where the siRNA fills the LNP interior (Figure 6F). Both would result in correlated scatter plots which we do not observe (dotted and dashed lines of Figure 6B).

Rather, our data are consistent with a weakly correlated scenario (Figure 6D), where self-assembled siRNA structures may be loaded in LNPs in a manner which is independent of LNP size. These measurements are consistent with a similar interpretation of cryo-TEM images of particles with similar compositions (see inset in Figure 6D).[27] Self-assembly of RNA structures is conjectured to be sensitive to properties, such as chemical modifications and length of RNA cargo, as well as to the ionic properties of the LNP environment and LNP composition. This analysis thus allows us to perform quantitative measurements of RNA-LNP size and loading properties and the relationship between them; measurements which are needed to understand and optimize a broad class of emerging genetic medicines.

Implications of Single-Particle Measurements of Size and Loading of LNPs. This work begins by benchmarking our tether-free, single-particle measurements of polystyrene nanoparticles with respect to the manufacturer's specifications and establishing agreement with the expected size within ±1 nm. This analysis involved developing single-particle tracking analysis methods suitable for measuring the diffusion coefficients of confined particle trajectories. Further, converting diffusion coefficient to size measurements required taking into account hydrodynamic effects associated with diffusion near surfaces. Performing measurements for a suite of particle sizes and microwell dimensions was important to validating

https://doi.org/10.1021/acsnano.1c04862
ACS Nano XXXX, XXX, XXX−XXX

our nano characterization approach, demonstrating quantitative agreement with other methods such as cryo-TEM and DLS. Despite limitations presented by the photobleaching of fluorescent labels, we are able to optimize our imaging settings to measure both diffusivity and loading of single particles. This is achieved by taking advantage of high single-to-noise ratios obtained with CLiC microscopy to track particles over long trajectories—with low excitation power—for particle sizing and measure single dye intensities—with much higher excitation power—for drug loading measurements.

The most exciting aspect of this study is the ability to measure the loading of drug molecules in delivery vehicles, with single-drug and single-particle resolution, at the same time as measuring single-particle diffusion and size. The ability to correlate a loading and diffusion/size measurement on every nanoparticle allows for the construction of the scatter plots and scaling coefficients described in Figures 2, 3, and 6, which give insights into the spatial distribution of molecules (or drugs) within the nanoparticles. Our technique is capable of delivering simultaneous size and loading information, with the power to discriminate between structural and spatial distribution hypotheses which are essential to understanding drug uptake and delivery mechanisms. To the best of our knowledge, we have developed the only single-particle technique that has demonstrated the ability to provide this information without tethering the particles or adhering them to surfaces and that can be extended to study dynamic changes in particle size and loading, in response to solution conditions such as pH. Dynamic change in these conditions is relevant to driving LNP uptake and drug release in cellular environments.

However, it should be noted that in the case of the 10 fluorophores/LNP formulation, the photobleaching measurements produced broad distributions. This could be explained by several factors including dye−dye interactions or photobleaching (see SI, Comparison of labeled drug loading distributions (Figures 5 and 6), for a detailed discussion). This an interesting subject for future inquiry and could potentially result in further refinement of this assay.

To date, cryo-TEM and NMR have been the dominant techniques for measuring indicators of the internal structure of nanoparticles. For example, the cryo-TEM data on ionizable LNPs have been used to show that the siRNA loading fraction can change the internal structure of these LNPs from unilamellar to multilamellar and back to unilamellar internal structure.[27] It is clear that dynamic structural rearrangements of LNPs are possible, which has implications toward how drugs are distributed through the LNPs in changing physiological contexts.

In fact, we obtain average sizes larger than those predicted by cryo-TEM images of the same LNPs, which was the comparative technique used by prior publications on the same LNP formulations.[27] Our diffusivity measurements correspond to smaller values—slower particles—than would be expected in the scenario where the LNPs were described by hard spheres with diameters reported by cryo-TEM. This discrepancy could arise for a variety of reasons, including the need for further development of the theoretical model to accommodate the more complex biophysical properties of the deformable LNPs with polymer exteriors (*i.e.*, the PEG brushes are expected to extend out to ∼4 nm around the nanoparticles)[48] and potential biases of cryo-TEM measurements. In comparing our measurements to cryo-TEM and other techniques, we recognize that different tools probe different measurable quantities and that "size" is a term used to describe more than one such quantify. Further, more sophisticated analyses are required to refine and interpret observations of increasingly complex materials, which are made in different contexts, such as diffusion is measured in solution, while cryo-TEM is performed using particles adhered to a surface.

Soft and structured materials such as LNPs may have more complex diffusive behavior than hard spheres, arising from nonelastic internal degrees of freedom. This may indicate a need for additional modifications of the transfer function eq 2 (modified Stokes−Einstein equation including hydrodynamic effects) that we used to compare our measurements to cryo-TEM. While the limited model that we used assumes a hard sphere moving through a viscous fluid, where thermal perturbations are converted into kinetic energy of the particle through elastic collisions, an expanded model could take into account the deformable nature of particles with their own viscosity, diffusing in a medium of different viscosity. This would also include the possibility for thermal perturbations from the medium to exchange energy with the particle's internal degrees of freedom through inelastic collisions.

In this regard, one outlook of this work is to perform quantitative studies of confinement effects and soft matter biophysics. This would especially apply to samples and environments of increasing biological complexity and physiological relevance, such as confined diffusion in the vicinity of artificial membranes, organelles, and living cells.

It is also worth noting that the samples used in our experiments are characterized by a range of siRNA loading which falls between the multilamellar-to-lamellar transition previously observed with cryo-TEM. Our measurements are consistent with neither surface nor volume loading but suggest the possibility of a localized cluster of aggregated siRNA whose size has only a weak dependence on the size of the LNP enveloping it. Previously, polarization enhanced NMR spectroscopy has been used to distinguish between homogeneous and heterogeneous shell−core models of LNP structure. The broadening of the NMR signal has suggested that siRNA becomes less mobile upon encapsulation.[32] While this may indicate that siRNA resides in the lipid phase of the LNPs, it is also consistent with localized siRNA aggregation as suggested in this work. Understanding of these structural properties of loaded LNPs, as a function of modifications to the siRNA cargo and LNP carrier, is the subject of future research and will be enriched by the methodology introduced in this work.

CONCLUSION

We have presented a single-particle, high-throughput nanocharacterization platform for size/diffusion and loading measurements of drug delivery vehicles. By analyzing many particles individually, we have obtained detailed distributions of particle size/diffusion and cargo loading. The ability to analyze the scaling of intensity with size has made it possible to distinguish between surface and volumetric distributions of cargo loading within LNPs as well as other more complex distributions. In the case of empty LNPs with labeled phospholipid headgroups, we measured a change from small, bilamellar micelles to larger, unilamellar vesicles induced by a change in pH. Analysis of cargo-loaded LNPs showed that siRNA loading increased the size of LNPs and suggested that the cargo may be aggregated in a cluster within the LNP rather than being uniformly distributed on the surface or through the volume of the LNP.

https://doi.org/10.1021/acsnano.1c04862
ACS Nano XXXX, XXX, XXX−XXX

Our technique allows us to perform size and loading experiments as a function of dynamic changes in solution conditions such as pH, since the entropic confinement of the nanoparticles in wells leaves a thin fluid layer for exchange of reagents during the single-particle imaging experiments. This work is broadly applicable to investigating microscopic and therapeutic properties of a wide range of nanomedicines, as a function of modifications to the drugs and vehicles. We hope that our contributions will help to accelerate the development of next generation of personalized medicines where a high level of resolution and analytical information is required to optimize performance.

MATERIALS AND METHODS

Sample Preparation: Polystyrene Nanoparticles. Carboxylate-modified polystyrene nanoparticles (Life Technologies, 48 ± 0.6 nm diameter[25] from EM analysis, excitation/emission = 505/515 nm) were purchased from ThermoFisher Scientific and are made with proprietary fluorescent labels. The nanoparticle samples were diluted to 1−2 nM, empirically determined concentrations for achieving a single particle per microwell. The dilutions were performed in serial steps 1:10, and samples were sonicated for at least 20 s at each dilution step. Finally, the samples were imaged at concentrations ranging from 0.82×10^7 to 8.2×10^7 particles·mL^{-1}.

Sample Preparation: Lipid Nanoparticles. Unloaded lipid nanoparticle (LNPs) formulations were prepared by the Cullis laboratory at the University of British Columbia, using the T-junction mixing technique.[27,33−35] This involved dissolving the 4 different lipid components, including KC2/Chol/DSPC/DSPE-PEG2000, in ethanol at a molar ratio of 50%/39%/10%/1% respectively, to a final concentration of 10 mM total lipid. Then using the T-junction mixer, the organic solution was then mixed with the appropriate aqueous buffer solution. In the case of unloaded LNPs, this was either 25 mM sodium acetate buffer (pH 4), or 1× phosphate buffered saline pH 7.4.

LNPs containing siRNA drugs were prepared as previously described,[27,34] using the T-junction mixer. Again the 4 lipid components (KC2/Chol/DSPC/DSPE-PEG2000) were dissolved in ethanol at a mixing ratio of 50%/39%/10%/1%. The organic solution was then rapidly mixed with an aqueous solution (25 mM sodium acetate pH 4) containing the siRNA drugs. The concentration of the siRNA drugs was chosen to achieve a high level of encapsulation with charge ratio N/P = 3.

The nanoparticle samples were prepared for imaging by diluting them in the respective buffers, as described above, to empirically determined concentrations for achieving single particles per microwell (approximately 1−2 nM LNP concentration).

Flow Cell Cleaning, Surface Treatment, and Assembly. The flow cell is made of two (25 mm × 25 mm) glass substrates separated by a 30 μm-thick double-sided adhesive (Nitto Denko, product no. 5603). The bottom layer of the flow cell, made of a 200 ± 10 μm-thick cover glass (Ted Pella, product no. 260452), contains an array of wells of varying diameters and depths, patterned by standard photolithography and dry-etched by reactive ion etching (RIE).[19] For measurements shown in Figure 1, the microwell diameter was 10 μm diameter, and the depth was varied from 200 to 1200 nm. In Figures 2, 3, and 6, the microwells used had 3 μm diameter and 500 nm depth, and for Figures 4 and 5, they had 3 μm diameter and 350 nm depth. The top layer of the flow cell, made of 150 ± 20 μm-thick standard microscope coverslips (VWR, product no. CA48366-089-1), has two holes drilled at opposing corners of the square, for sample introduction.

Both top and bottom coverslips of each flow cell were passivated with PEG layers using silane chemistry, an amine-thiol cross-linker and a cloud point PEGylation technique previously described in literature.[36] The procedure starts with cleaning of the flow cell layers using sonication in acetone and isopropanol prior to piranha cleaning of 30 min (at a 3:1 mixing ratio of sulfuric acid and hydrogen peroxide). Then, 3-(aminopropyl)triethoxysilane was vapor phase deposited[37] inside a vacuum desiccator at around 1.5 Torr for 30 min at room temperature, followed by an annealing step at 120 °C for 20 min on a hot plate, resulting in primary amines covering the flow cell layer surface. A solution of sulfo-SMCC (4-(*N*-maleimidomethyl)-cyclohexane-1-carboxylic acid 3-sulfo-*N*-hydroxysuccinimide ester) cross-linker at 2 mg/mL in 10× diluted phosphate buffered saline (15 mM salt concentration) was left to react with the aminated flow cell layers for 30 min at room temperature. Finally, the flow cell layers were exposed to a solution of thiol-PEG in 0.9 M Na_2SO_4 for at least 48 h, forming a PEG passivation layer on the surface. The coverslips were then rinsed thoroughly three times with deionized (DI) water and blow-dried with high-purity nitrogen before flow cell assembly. The assembled flow cell is then sealed in a custom microfluidic chuck.[16]

Single-Molecule CLiC Microscopy. The microscopy setup and imaging were performed using fluorescent microscopy in combination with CLiC.[15] Briefly, a microfluidic chuck for sample exchange was used to hold the flow cell on a microscope sample plate, located between the objective and the CLiC pusher lens (Figure 1 A). The imaging system included a Nikon Ti-E inverted microscope, Andor iXon Ultra 897 EMCCD camera, and a coherent Sapphire 532 nm-150 mW LP laser system. The bottom coverslip was patterned with arrays of cylindrical, open face microwells (Figure 1A(i)) within which the nanoparticles were laterally confined (Figure 1A(ii,iii),B), as the two coverslips were deflected and brought into contact.

During the experiments, the CLiC lens was lowered and raised repeatedly to trap and refresh the wells with fresh particles from the bulk solution. This allowed for quantitative measurements of a statistically relevant number of individual nanoparticles, which is important for characterizing heterogeneous samples. Videos of single particle trajectories (Figure 1B,C(i)) were collected using the Andor camera with either 40× (Plan Fluor 40× oil immersion objective lens, N.A. 1.3, W.D. 0.2 mm, F.O.V. 25 mm, in Figure 1 and S1) or 100× (Apochromat TIRF 100× oil immersion objective lens N.A. 1.49, W.D. 0.12 mm, F.O.V 22 mm, in Figures 2−6) magnifications (on-camera pixel size was 16 μm/pixel). Optimal imaging parameters such as exposure time and laser power were chosen with feedback from variance and bias values obtained from computer simulations of particles diffusing in a 2D Gaussian light intensity profile under, a circular well confinement with a known diffusion coefficient. This procedure led us to choose 600 frames (at 20 ms exposure and 5 mW laser power) for polystyrene nanoparticles (Figure 1) and 2000 frames (at 6 ms exposure and 5 mW laser power) for LNPs (Figures 2, 3, and 6). In the case of the photobleaching experiments (Figures 4 and 5), at least 6000 frames were collected at 2 ms exposure time and 8 mW laser power. Here, the laser beam diameter was demagnified by 15× to increase power density and hence optimize SNR for bleaching step measurements. For the measurements, the EM-gain of the Andor camera was set at 300.

Single-Particle Trajectory Analysis to Determine Diffusivity. To measure the size and intensity of single-particles, we employed single-particle identification, tracking, and a mean-squared displacement (MSD) analysis adapted for confined diffusion in a circular geometry. Wells with single diffusing particles were identified (details in SI, Pyramid approach to particle detection) and used for analysis, while wells containing multiple particles were excluded. Single-particle tracking (SPT) was then applied to each individual well.[38,39] Localization of the single diffusing particle was achieved by fitting the signal in each frame with a 2D symmetric Gaussian[40−42] (Figure 1C(ii)). Trajectories were obtained by compiling successive positions obtained on each frame.

To determine the diffusion coefficients, empirical MSD points were generated for increasing time lags from SPT trajectories using eq S3 in SI. The points are shown in Figure 1D. The diffusion coefficients are extracted by fitting with a theoretical confined MSD model for circular confinement.[43] We additionally modified the existing 2D circular confinement MSD model for fitting, as the finite exposure time effect and shot noise are expected to contribute in the form of an offset.[44] For long time scales, the MSD curve saturates, and this is

https://doi.org/10.1021/acsnano.1c04862
ACS Nano XXXX, XXX, XXX−XXX

characteristic of the particle experiencing confined diffusion due to the microwell. At short time scales, the particle undergoes free diffusion, and the MSD curve is approximately linear. Further information is provided in the SI.

Single-Particle Diffusivity Analysis to Determine Size. Normally the Stokes−Einstein equation is invoked to transform diffusion coefficient (D_0) to hydrodynamic radius (a):

$$a = \frac{k_B T}{6\pi\eta D_0} \tag{3}$$

where k_B is the Boltzmann constant, T is the temperature, and η is kinetic viscosity of the solution. Because our measurements are taken under confined conditions where the size of the particle can be a significant fraction of the vertical dimension of our microwell, we must correct for the effect of hydrodynamic forces acting near the top and bottom confining surfaces. When the particle is near a surface, it slows significantly, resulting in lower diffusion coefficients which would result in diameters that are too large if the unmodified Stokes−Einstein equation was used. We use the following eq 2 (shown in the Results and Discussion section), for the diffusion coefficient $D_{\parallel}$ measured near to parallel confinement surfaces. λ is the correction factor for diffusivity of particles confined between two parallel walls with a separation distance d_w. For a particle midway between the walls, with a radius $a = d/2$, λ can be obtained as a polynomial expansion in a/z:[24,45]

$$\lambda^{-1} = 1 - 1.004\left(\frac{a}{z}\right) + 0.418\left(\frac{a}{z}\right)^3 + 0.21\left(\frac{a}{z}\right)^4 - 0.169\left(\frac{a}{z}\right)^5 + O\left(\frac{a}{z}\right)^6 \tag{4}$$

where $z = d_w/2$ is the midway distance between the two planes of confinement. We use a series of experiments (Figure S1 and Table 2, SI) with varying confinement heights to fit for the correction factor (see SI, Corrections for size measurement under parallel planes of confinement, for details). By doing this, we are able to use information from measurements at all confinement depths to yield a particle size that best fits all the data.

Photobleaching Analysis for Cargo Loading. We used a stepwise photobleaching approach to count the fluorophores attached to a given molecule or nanoparticle. While this is easier to implement compared to other advanced statistical methods, it can be hard to detect photobleaching steps when the total number of fluorophores is large, or the signal-to-noise ratio is low. Therefore, the method used here should only be used when the average number of fluorophores per particle is small or the last photobleaching steps are easily distinguishable. On the other hand, when the average number of fluorophores is large, advanced methods should be used (*i.e.*, Bayesian counting methods).[46,47] Fortunately, given the fast-imaging time scales used (at frame rate of 2 ms as shown Figure 4A,D,G) for intensity traces obtained using the CLiC platform, any fluorophore counting method using raw intensities can be used.

A particle labeled with multiple fluorophores shows stepwise drops in intensity, corresponding to independent photobleaching events. These intensity steps are detected using an algorithm reported by Chen *et al.*,[31] which is based on the two-sample t test edge detection. Due to noise in the intensity trace, the edge detector will sometimes miss transition times and count multiple steps as a single one. This is evident in the increasing skewness of the single bleaching step distributions (Figure 4D−F). By using kernel density estimation to fit the distribution of these intensity steps, we can accurately find and avoid overestimating the unit step size ΔI of a single photobleaching event (details in SI, Analysis Method: Particle loading). To determine the number of fluorophores per particle, we divide the total change in particle intensity by the unit step size of a single fluorophore.

ASSOCIATED CONTENT

Supporting Information

The Supporting Information is available free of charge at https://pubs.acs.org/doi/10.1021/acsnano.1c04862.

Comparisons with other sizing techniques; particle detection, tracking and sizing; LNP cargo-loading distributions; simulation of confined particles (PDF)

AUTHOR INFORMATION

Corresponding Author

Sabrina Leslie − *Michael Smith Laboratories and Department of Physics, University of British Columbia, Vancouver, British Columbia, Canada V6T 1Z4; Department of Physics, McGill University, Montreal, Quebec, Canada H3A2T8; Department of Physics Astronomy, University of British Columbia, Vancouver, British Columbia, Canada V6T 1Z1;* orcid.org/0000-0003-4336-0447; Email: sabrina.leslie@msl.ubc.ca

Authors

Albert Kamanzi − *Department of Physics, McGill University, Montreal, Quebec, Canada H3A2T8; Department of Physics Astronomy, University of British Columbia, Vancouver, British Columbia, Canada V6T 1Z1; Michael Smith Laboratories and Department of Physics, University of British Columbia, Vancouver, British Columbia, Canada V6T 1Z4;* orcid.org/0000-0002-6790-1140

Yifei Gu − *Department of Physics, McGill University, Montreal, Quebec, Canada H3A2T8;* orcid.org/0000-0003-1507-0258

Radin Tahvildari − *Department of Physics, McGill University, Montreal, Quebec, Canada H3A2T8*

Zachary Friedenberger − *Department of Physics, McGill University, Montreal, Quebec, Canada H3A2T8*

Xingqi Zhu − *Department of Physics, McGill University, Montreal, Quebec, Canada H3A2T8*

Romain Berti − *ScopeSys Inc., Montreal, Quebec, Canada H3C 2M7; Department of Physics, McGill University, Montreal, Quebec, Canada H3A2T8; Michael Smith Laboratories and Department of Physics, University of British Columbia, Vancouver, British Columbia, Canada V6T 1Z4*

Marty Kurylowicz − *ScopeSys Inc., Montreal, Quebec, Canada H3C 2M7; Department of Physics, McGill University, Montreal, Quebec, Canada H3A2T8*

Dominik Witzigmann − *Department of Biochemistry and Molecular Biology, University of British Columbia, Vancouver, British Columbia, Canada V6T 1Z4;* orcid.org/0000-0002-8197-8558

Jayesh A. Kulkarni − *Department of Biochemistry and Molecular Biology, University of British Columbia, Vancouver, British Columbia, Canada V6T 1Z4;* orcid.org/0000-0002-3622-6998

Jerry Leung − *Department of Biochemistry and Molecular Biology, University of British Columbia, Vancouver, British Columbia, Canada V6T 1Z4*

John Andersson − *Department of Chemistry and Chemical Engineering, Chalmers University of Technology, SE-412 96 Gothenburg, Sweden;* orcid.org/0000-0002-2977-8305

Andreas Dahlin − *Department of Chemistry and Chemical Engineering, Chalmers University of Technology, SE-412 96 Gothenburg, Sweden*

Fredrik Höök − *Department of Physics, Chalmers University of Technology, SE-412 96 Gothenburg, Sweden;* orcid.org/0000-0003-1994-5015

Mark Sutton − *Department of Physics, McGill University, Montreal, Quebec, Canada H3A2T8*

https://doi.org/10.1021/acsnano.1c04862
ACS Nano XXXX, XXX, XXX−XXX

Pieter R. Cullis − *Department of Biochemistry and Molecular Biology, University of British Columbia, Vancouver, British Columbia, Canada V6T 1Z4;* orcid.org/0000-0001-9586-2508

Complete contact information is available at: https://pubs.acs.org/10.1021/acsnano.1c04862

Author Contributions

○These authors contributed equally to this work.

Notes

The authors declare the following competing financial interest(s): S.L. has financial interest in Scopesys Inc. P.R.C. has financial interest in Acuitas and PrecisionNanosystems. All the three companies mentioned above are active in the space of lipid nanoparticle development. The remaining authors declare no conflict of interest.

ACKNOWLEDGMENTS

The authors acknowledge technical, operational, and financial support from a number of sources. Several members of the Leslie laboratory and collaborators contributed to the work. This includes Z. Zhang who contributed background theory to this work, which was published in his M.Sc. thesis. Former undergraduate students in the Leslie laboratory: H. Liao, Y. Patel, Y. Ji, and S. Chen also contributed to the project. Further to this, Dr. D. Berard supported aspects of the technical research and Dr. K. Metera supported communication aspects of the project. Dr. M. Shayegan took data with a different class of nanoparticles which preceded this work and helped validate its continuation. Operational support of the research laboratory was provided by department technicians R. Talbot, R. Gagnon, and J. Smeros at McGill Physics. Further, the McGill Nanotools facility provided fabrication infrastructure for constructing the flow cells. Funding for this work was provided by the NSERC Idea to Innovation research programs (Phase 1 and 2), the NSERC Accelerator award, the NSERC Discovery program, the NSERC Alliance − COVID-19 award, the NMIN Strategic Initiative at UBC, and Mitacs fellowships, all in partnership with ScopeSys, a company spun out of the Leslie laboratory.

REFERENCES

(1) Torchilin, V. Multifunctional Nanocarriers. *Adv. Drug Delivery Rev.* **2006**, *58*, 1532−1555.

(2) Puri, A.; Loomis, K.; Smith, B.; Lee, J.; Yavlovich, A.; Heldman, E.; Blumenthal, R. Lipid-Based Nanoparticles as Pharmaceutical Drug Carriers: From Concepts to Clinic. *Crit. Rev. Ther. Drug Carrier Syst.* **2009**, *26*, 523−80.

(3) Cullis, P. R.; Hope, M. J. Lipid Nanoparticles Systems for Enabling Gene Therapies. *Mol. Ther.* **2017**, *25*, 1467−1475.

(4) Kulkarni, J. A.; Cullis, P. R.; van der Meel, R. Lipid Nanoparticles Enabling Gene Therapies: From Concepts to Clinical Utility. *Nucleic Acid Ther.* **2018**, *28*, 146−157.

(5) Goodsell, D. S. Bionanotechnology: *Lessons from Nature*; John Wiley & Sons: Hoboken, NJ, 2004.

(6) Leung, A. K.; Tam, Y. Y.; Chen, S.; Hafez, I. M.; Cullis, P. R. Microfluidic Mixing: A General Method for Encapsulating Macromolecules in Lipid Nanoparticle Systems. *J. Phys. Chem. B* **2015**, *119*, 8698−8706.

(7) Reichmuth, A. M.; Oberli, M. A.; Jaklenec, A.; Langer, R.; Blankschtein, D. mRNA Vaccine Delivery Using Lipid Nanoparticles. *Ther. Delivery* **2016**, *7*, 319−34.

(8) McKay, P. F.; Hu, K.; Blakney, A. K.; Samnuan, K.; Brown, J. C.; Penn, R.; Zhou, J.; Bouton, C. R.; Rogers, P.; Polra, K.; Lin, P. J. C.; Barbosa, C.; Tam, Y. K.; Barclay, W. S.; Shattock, R. J. Self-Amplifying RNA SARS-CoV-2 Lipid Nanoparticle Vaccine Candidate Induces High Neutralizing Antibody Titers in Mice. *Nat. Commun.* **2020**, *11*, 3523.

(9) Witzigmann, D.; Kulkarni, J. A.; Leung, J.; Chen, S.; Cullis, P. R.; van der Meel, R. Lipid Nanoparticle Technology for Therapeutic Gene Regulation in the Liver. *Adv. Drug Delivery Rev.* **2020**, *159*, 344−363.

(10) Patel, S.; Ryals, R. C.; Weller, K. K.; Pennesi, M. E.; Sahay, G. Lipid Nanoparticles for Delivery of Messenger RNA to the Back of the Eye. *J. Controlled Release* **2019**, *303*, 91−100.

(11) Jayaraman, M.; Ansell, S. M.; Mui, B. L.; Tam, Y. K.; Chen, J.; Du, X.; Butler, D.; Eltepu, L.; Matsuda, S.; Narayanannair, J. K.; Rajeev, K. G.; Hafez, I. M.; Akinc, A.; Maier, M. A.; Tracy, M. A.; Cullis, P. R.; Madden, T. D.; Manoharan, M.; Hope, M. J. Maximizing the Potency of siRNA Lipid Nanoparticles for Hepatic Gene Silencing *in Vivo*. *Angew. Chem.* **2012**, *124*, 8657−8661.

(12) Semple, S. C.; Akinc, A.; Chen, J.; Sandhu, A. P.; Mui, B. L.; Cho, C. K.; Sah, D. W.; Stebbing, D.; Crosley, E. J.; Yaworski, E.; Hafez, I. M.; Dorkin, J. R.; Qin, J.; Lam, K.; Rajeev, K. G.; Wong, K. F.; Jeffs, L. B.; Nechev, L.; Eisenhardt, M. L.; Jayaraman, M.; et al. Rational Design of Cationic Lipids for siRNA Delivery. *Nat. Biotechnol.* **2010**, *28*, 172−176.

(13) Lv, H.; Zhang, S.; Wang, B.; Cui, S.; Yan, J. Toxicity of Cationic Lipids and Cationic Polymers in Gene Delivery. *J. Controlled Release* **2006**, *114*, 100−109.

(14) Leslie, S. R.; Fields, A. P.; Cohen, A. E. Convex Lens-Induced Confinement for Imaging Single Molecules. *Anal. Chem.* **2010**, *82*, 6224−9.

(15) Berard, D.; McFaul, C. M. J.; Leith, J. S.; Arsenault, A. K. J.; Michaud, F.; Leslie, S. R. Precision Platform for Convex Lens-Induced Confinement Microscopy. *Rev. Sci. Instrum.* **2013**, *84*, 103704.

(16) Berard, D. J.; Shayegan, M.; Michaud, F.; Henkin, G.; Scott, S.; Leslie, S. Formatting and Ligating Biopolymers Using Adjustable Nanoconfinement. *Appl. Phys. Lett.* **2016**, *109*, 033702.

(17) Leith, J. S.; Kamanzi, A.; Sean, D.; Berard, D.; Guthrie, A. C.; McFaul, C. M.; Slater, G. W.; de Haan, H. W.; Leslie, S. R. Free Energy of a Polymer in Slit-Like Confinement from the Odijk Regime to the Bulk. *Macromolecules* **2016**, *49*, 9266−9271.

(18) Berard, D. J.; Michaud, F.; Mahshid, S.; Ahamed, M. J.; McFaul, C. M. J.; Leith, J. S.; Bérubé, P.; Sladek, R.; Reisner, W.; Leslie, S. R. Convex Lens-Induced Nanoscale Templating. *Proc. Natl. Acad. Sci. U. S. A.* **2014**, *111*, 13295−300.

(19) Henkin, G.; Berard, D.; Stabile, F.; Shayegan, M.; Leith, J. S.; Leslie, S. R. Manipulating and Visualizing Molecular Interactions in Customized Nanoscale Spaces. *Anal. Chem.* **2016**, *88*, 11100−11107.

(20) Scott, S.; Xu, Z. M.; Kouzine, F.; Berard, D. J.; Shaheen, C.; Gravel, B.; Saunders, L.; Hofkirchner, A.; Leroux, C.; Laurin, J.; Levens, D.; Benham, C.; Leslie, S. Visualizing Structure-Mediated Interactions in Supercoiled DNA Molecules. *Nucleic Acids Res.* **2018**, *46*, 4622−4631.

(21) Scott, S.; Shaheen, C.; McGuinness, B.; Metera, K.; Kouzine, F.; Levens, D.; Benham, C. J; Leslie, S. Single-Molecule Visualization of the Effects of Ionic Strength and Crowding on Structure-Mediated Interactions in Supercoiled DNA Molecules. *Nucleic Acids Res.* **2019**, *47*, 6360−6368.

(22) Shayegan, M.; Tahvildari, R.; Metera, K.; Kisley, L.; Michnick, S. W.; Leslie, S. R. Probing Inhomogeneous Diffusion in the Microenvironments of Phase-Separated Polymers under Confinement. *J. Am. Chem. Soc.* **2019**, *141*, 7751−7757.

(23) Life Technologies *Fluospheres Fluorescent Color Kit, Carboxylate-Modified microspheres, 0.04 μm , 5% solids*, cat. no. F-10720. https://www.thermofisher.com/order/catalog/product/F10720 (accessed 2021-10-20).

(24) Lin, B.; Yu, J.; Rice, S. A. Direct Measurements of Constrained Brownian Motion of an Isolated Sphere between Two Walls. *Phys. Rev. E: Stat. Phys., Plasmas, Fluids, Relat. Interdiscip. Top.* **2000**, *62*, 3909.

(25) Benesch, T.; Yiacoumi, S.; Tsouris, C. Brownian Motion in Confinement. *Phys. Rev. E: Stat. Phys., Plasmas, Fluids, Relat. Interdiscip. Top.* **2003**, *68*, 021401.
(26) Bian, X.; Kim, C.; Karniadakis, G. E. 111 Years of Brownian Motion. *Soft Matter* **2016**, *12*, 6331−6346.
(27) Kulkarni, J. A.; Darjuan, M. M.; Mercer, J. E.; Chen, S.; Van Der Meel, R.; Thewalt, J. L.; Tam, Y. Y. C.; Cullis, P. R. On the Formation and Morphology of Lipid Nanoparticles Containing Ionizable Cationic Lipids and siRNA. *ACS Nano* **2018**, *12*, 4787−4795.
(28) Wan, C.; Allen, T.; Cullis, P. Lipid Nanoparticle Delivery Systems for siRNA Based Therapeutics. *Drug Delivery Transl. Res.* **2014**, *4*, 74−83.
(29) Kulkarni, J. A.; Witzigmann, D.; Leung, J.; van der Meel, R.; Zaifman, J.; Darjuan, M. M.; GrischChan, H. M.; Thöny, B.; Tam, Y. Y. C.; Cullis, P. R. Fusion-Dependent Formation of Lipid Nanoparticles Containing Macromolecular Payloads. *Nanoscale* **2019**, *11*, 9023−9031.
(30) Kulkarni, J. A.; Witzigmann, D.; Chen, S.; Cullis, P. R.; van der Meel, R. Lipid Nanoparticle Technology for Clinical Translation of siRNA Therapeutics. *Acc. Chem. Res.* **2019**, *52*, 2435−2444.
(31) Chen, Y.; Deffenbaugh, N. C.; Anderson, C. T.; Hancock, W. O. Molecular Counting by Photobleaching in Protein Complexes with Many Subunits: Best Practices and Application to the Cellulose Synthesis Complex. *Mol. Biol. Cell* **2014**, *25*, 3630−3642.
(32) Viger-Gravel, J.; Schantz, A.; Pinon, A. C.; Rossini, A. J.; Schantz, S.; Emsley, L. Structure of Lipid Nanoparticles Containing siRNA or mRNA by Dynamic Nuclear Polarization-Enhanced NMR Spectroscopy. *J. Phys. Chem. B* **2018**, *122*, 2073−2081.
(33) Hirota, S.; de Ilarduya, C. T.; Barron, L. G.; Szoka, F. C., Jr Simple Mixing Device to Reproducibly Prepare Cationic Lipid-DNA Complexes (Lipoplexes). *BioTechniques* **1999**, *27*, 286−290.
(34) Jeffs, L. B.; Palmer, L. R.; Ambegia, E. G.; Giesbrecht, C.; Ewanick, S.; MacLachlan, I. A Scalable, Extrusion-Free Method for Efficient Liposomal Encapsulation of Plasmid DNA. *Pharm. Res.* **2005**, *22*, 362−372.
(35) Kulkarni, J. A.; Tam, Y. Y. C.; Chen, S.; Tam, Y. K.; Zaifman, J.; Cullis, P. R.; Biswas, S. Rapid Synthesis of Lipid Nanoparticles Containing Hydrophobic Inorganic Nanoparticles. *Nanoscale* **2017**, *9*, 13600−13609.
(36) Emilsson, G.; Schoch, R. L.; Feuz, L.; Hook, F.; Lim, R. Y.; Dahlin, A. B. Strongly Stretched Protein Resistant Poly(ethylene Glycol) Brushes Prepared by Grafting-To. *ACS Appl. Mater. Interfaces* **2015**, *7*, 7505−7515.
(37) Yuan, X.; Wolf, N.; Mayer, D.; Offenhausser, A.; Wordenweber, R. Vapor-Phase Deposition and Electronic Characterization of 3-Aminopropyltriethoxysilane Self-Assembled Monolayers on Silicon Dioxide. *Langmuir* **2019**, *35* (25), 8183−8190.
(38) Shen, H.; Tauzin, L. J.; Baiyasi, R.; Wang, W.; Moringo, N.; Shuang, B.; Landes, C. F. Single Particle Tracking: From Theory to Biophysical Applications. *Chem. Rev.* **2017**, *117*, 7331−7376.
(39) Manzo, C.; Garcia-Parajo, M. F. A Review of Progress in Single Particle Tracking: From Methods to Biophysical Insights. *Rep. Prog. Phys.* **2015**, *78* (12), 124601.
(40) Cheezum, M. K.; Walker, W. F.; Guilford, W. H. Quantitative Comparison of Algorithms for Tracking Single Fluorescent Particles. *Biophys. J.* **2001**, *81*, 2378−2388.
(41) Anderson, C.; Georgiou, G.; Morrison, I.; Stevenson, G.; Cherry, R. Tracking of Cell Surface Receptors by Fluorescence Digital Imaging Microscopy Using a Charge-Coupled Device Camera. Low Density Lipoprotein and Influenza Virus Receptor Mobility at 4 Degrees C. *J. Cell Sci.* **1992**, *101*, 415−425.
(42) Schütz, G.; Schindler, H.; Schmidt, T. Single-Molecule Microscopy on Model Membranes Reveals Anomalous Diffusion. *Biophys. J.* **1997**, *73*, 1073−1080.
(43) Bickel, T. A. Note on Confined Diffusion. *Phys. A (Amsterdam, Neth.)* **2007**, *377*, 24−32.
(44) Michalet, X. Mean Square Displacement Analysis of Single-Particle Trajectories with Localization Error: Brownian Motion in an Isotropic Medium. *Phys. Rev. E* **2010**, *82*, 041914.
(45) Happel, J.; Brenner, H. *Low Reynolds Number Hydrodynamics*; Martinus Nijhoff Publisher: The Hague, 1983.
(46) Tsekouras, K.; Custer, T. C.; Jashnsaz, H.; Walter, N. G.; Pressé, S. A Novel Method to Accurately Locate and Count Large Numbers of Steps by Photobleaching. *Mol. Biol. Cell* **2016**, *27*, 3601−3615.
(47) Garry, J.; Li, Y.; Shew, B.; Gradinaru, C. C.; Rutenberg, A. D. Bayesian Counting of Photobleaching Steps with Physical Priors. *J. Chem. Phys.* **2020**, *152*, 024110.
(48) Allen, C.; Dos Santos, N.; Gallagher, R.; Chiu, G. N. C.; Shu, Y.; Li, W. M.; Johnstone, S. A.; Janoff, A. S.; Mayer, L. D.; Webb, M. S.; Bally, M. B. Controlling the Physical Behavior and Biological Performance of Liposome Formulations through Use of Surface Grafted Poly(ethylene Glycol). *Biosci. Rep.* **2002**, *22* (2), 225−250.
(49) ThermoFisher Scientific *Dil Stain (1,1′-Dioctadecyl-3,3,3′,3′-tetramethylindocarbocyanine Perchlorate (DiI; DiIC18(3)))*. https://www.thermofisher.com/order/catalog/product/D3911#/D3911 (accessed 2021-10-20).
(50) Integrated DNA Technologies *TYE 563 Transfection Control siRNA, 1 nmol*, cat. no. 51-01-20-19) https://www.idtdna.com/pages/products/functional-genomics/dsirnas-and-trifecta-rnai-kits (accessed 2021-10-20).

https://doi.org/10.1021/acsnano.1c04862
ACS Nano XXXX, XXX, XXX−XXX